crystals

MDPI

*Article*

# Crystallographic and TEM Features of a TBC/$Ti_2AlC$ MAX Phase Interface after 1300 °C Burner Rig Oxidation

**James L. Smialek *, Anita Garg, Bryan J. Harder and Michael D. Cuy**

NASA Glenn Research Center, Cleveland, OH 44135, USA; bryan.harder@nasa.gov (B.J.H.)
* Correspondence: dr.jsmialek@outlook.com

**Abstract:** A FIB/STEM interfacial study was performed on a TBC/$Ti_2AlC$ MAX phase system, oxidized in an aggressive burner rig test (Mach 0.3 at 1300 °C for 500 h). The 7YSZ TBC, $\alpha$-$Al_2O_3$ TGO, and MAXthal 211™ $Ti_2AlC$ base were variously characterized by TEM/STEM, EDS, SADP, and HRTEM. The YSZ was a mix of "clean" featureless and "faulted" high contrast grains. The latter exhibited ferro-elastic domains of high Y content tetragonal **t"** variants. No martensite was observed. The TGO was essentially a duplex $\alpha$-$Al_2O_3$ structure of inner columnar plus outer equiaxed grains. It maintained a perfectly intact, clean interface with the $Ti_2AlC$ substrate. The $Ti_2AlC$ substrate exhibited no interfacial Al-depletion zone but, rather, numerous faults along the basal plane of the hexagonal structure. These are believed to offer a means of depleting Al by forming crystallographic, low-Al planar defects, proposed as $Ti_{2.5}AlC_{1.5}$. These characterizations support and augment prior optical, SEM, and XRD findings that demonstrated remarkable durability for the YSZ/$Ti_2AlC$ MAX phase system in aggressive burner tests.

**Keywords:** $Ti_2AlC$; YSZ TBC; $Al_2O_3$ TGO; burner oxidation; FIB TEM/STEM



**Citation:** Smialek, J.L.; Garg, A.; Harder, B.J.; Cuy, M.D. Crystallographic and TEM Features of a TBC/$Ti_2AlC$ MAX Phase Interface after 1300 °C Burner Rig Oxidation. *Crystals* **2023**, *13*, 691. https://doi.org/10.3390/cryst13040691

Academic Editor: Daniel Errandonea

Received: 30 March 2023
Revised: 11 April 2023
Accepted: 12 April 2023
Published: 17 April 2023



## 1. Introduction

Thermal barrier coatings (TBC) are widely used and studied for turbine airfoil applications [1]; these generally employed Ni-base superalloys with a maximum use temperature of 1150 °C. This limitation is dictated by the creep properties of the metal and the spallation tendency of the TBC and thermally grown oxide (TGO) scale. The latter is primarily $\alpha$-$Al_2O_3$ formed on oxidation-resistant Ni(Pt)Al or Ni(Co)CrAlY bond coats. It is driven toward failure by a coefficient of thermal expansion mismatch with the substrate alloys. Since higher temperatures produce greater operational efficiencies, studies are often directed toward systems allowing greater use of temperature. One example is using novel substrates with exceptional oxidation resistance [2]. In this regard, more recent substrates that exhibit excellent oxidation resistance are the $Al_2O_3$—forming $Ti_2AlC$ and $Cr_2AlC$ MAX phases. Furthermore, these substrates have close thermal expansion matches with $\alpha$-$Al_2O_3$ and YSZ, and provide motivation to explore TBC durability [3,4]. These initial demonstrations, provided by furnace tests, indeed showed that TBC/MAX phase systems could survive orders of magnitude longer than conventional superalloy systems. Consequently, follow-on works employed even more demanding burner rig tests [5,6].

The present study elaborates on some microstructural features exhibited in polished cross-sections of a burner-tested TBC/$Ti_2AlC$ system. Here, the durability of a plasma sprayed, physical vapor deposited (PS-PVD) 7 wt.% yttria-stabilized zirconia (7YSZ) thermal barrier coating (TBC) on an alumina-forming $Ti_2AlC$ MAX phase was investigated in a high-velocity Mach 0.3 (~100 m/s) burner test, burning Jet A fuel at atmospheric pressure. The system survived 500 h at an external surface temperature of 1300 °C, using 5-h cycles, with no backside cooling. Oxidation was modest, gaining just 2.4 mg/cm$^2$ and exhibiting well-behaved cubic-linear kinetics (Figure 1) [5].

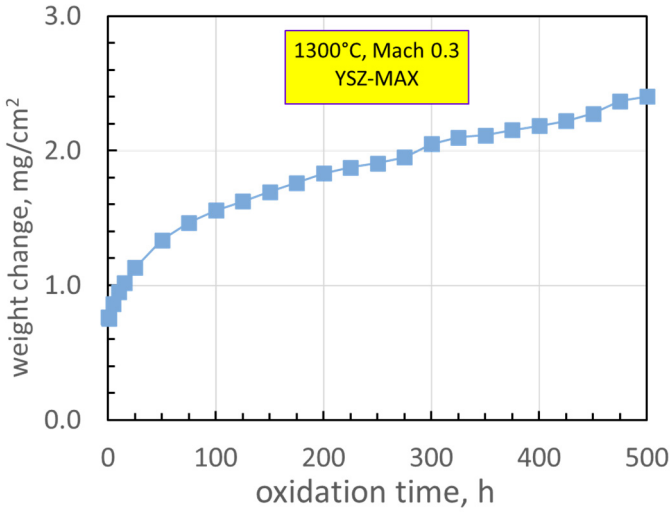


**Figure 1.** Weight change performance of YSZ-coated $Ti_2AlC$ MAX phase in 1300 °C Mach 0.3 burner test. (from Smialek et al., 2020 [5]).

No indication of TBC failure or spallation was apparent. This was compared to furnace cycling of commercial TBC-Ni(Pt)Al bondcoat–superalloy systems with only 30 h life projected at 1300 °C, and withstanding only 7 μm of thermally grown $Al_2O_3$ TGO [7]. For the 500 h YSZ-MAX phase burner test, optical and scanning electron microscopy (SEM) microstructural analyses revealed an intact 22 μm $Al_2O_3$ scale under the TBC, at the hot gas impingement face, and approximately 14 μm on the bare backside. The exposed backside was somewhat cooler at 1216 °C and subject to scale volatility, exhibiting a filamentary, etched scale surface structure with signs of Ti- and Al-oxide attack by moisture-induced volatilization. The frontside YSZ coating underwent sintering and some phase migration to high-Y cubic and low-Y tetragonal, as demonstrated by Rietveld XRD analyses. The expected transformation of low-Y (t) phase to the detrimental monoclinic phase, associated with the TBC spallation and delamination, was not observed. The present focused ion beam—scanning transmission electron microscopy (FIB-STEM) study was initiated to support and enlarge upon those microstructural and XRD phase findings, but in greater detail.

## 2. Materials and Methods

The material, coating, and burner test have been described in detail [8]. Briefly, Kanthal/Sandvik MAXthal 211™ $Ti_2AlC$ material was sectioned from a sintered slab and coated in the Sulzer–Oerlikon–Metco plasma spray physical vapor deposition (PS-PVD) facility at the NASA Glenn Research Center. The burner rig utilized 120 psig (800 kPa) filtered shop air and approximately 1.1 kg (2.5 lb)/min airflow, preheated and mixed with atomized Jet-A fuel. Combustor pressure was 1 psi (6.9 kPa) above ambient to produce a Mach 0.3 flame velocity through a 1 in. (2.54 cm) exit nozzle. The flame temperature was monitored by thermocouple, sample temperature by optical pyrometer (8 μm wavelength for YSZ, emissivity set at 0.92, and 2-color pyrometer for bare $Ti_2AlC$) controlled ±5 °C by a feedback loop. The YSZ-$Ti_2AlC$ interface was estimated as 1244 °C and the bare backside was measured as 1216 °C. Cycling every 5 h was produced by pivoting the burner apparatus. Inspections and weighing occurred at 1, 10, 15, and 25 h, then every 25 h thereafter, as measured on an analytical balance sensitive to 0.01 mg.

The burner and sample are shown in Figure 2. The YSZ coating was exposed face-on (arrow) to the hot gas exhaust of the burner. The 1300 °C test control coating surface temperature was targeted at the centerline of the hot zone. The schematic (Figure 2b) illustrates the arrangement of the Ni-plating, YSZ TBC top coat, $Al_2O_3$ scale (TGO), and $Ti_2AlC$ substrate in the polished cross-section with respect to hot gas impingement (arrow). Finally, a montage of the full cross-section (SEM/BSE, Figure 2c) shows actual microstructural

features. The positions of the ~20 µm long FIB sections were across the TGO at both front and back faces, incorporating interfaces with the TBC and $Ti_2AlC$ matrix. These site-specific sections (TEM foils) at the coated front and uncoated backside were fibbed out using a ZEISS Auriga dual focused ion beam (FIB)/SEM microscope, and are marked as "FIB, I" and "FIB, II", resp. in Figure 2. The TEM foils were then examined in a Thermo-Fisher Talos F200S scanning/transmission electron microscope (S/TEM) for detailed microstructural, phase, and chemical analyses.

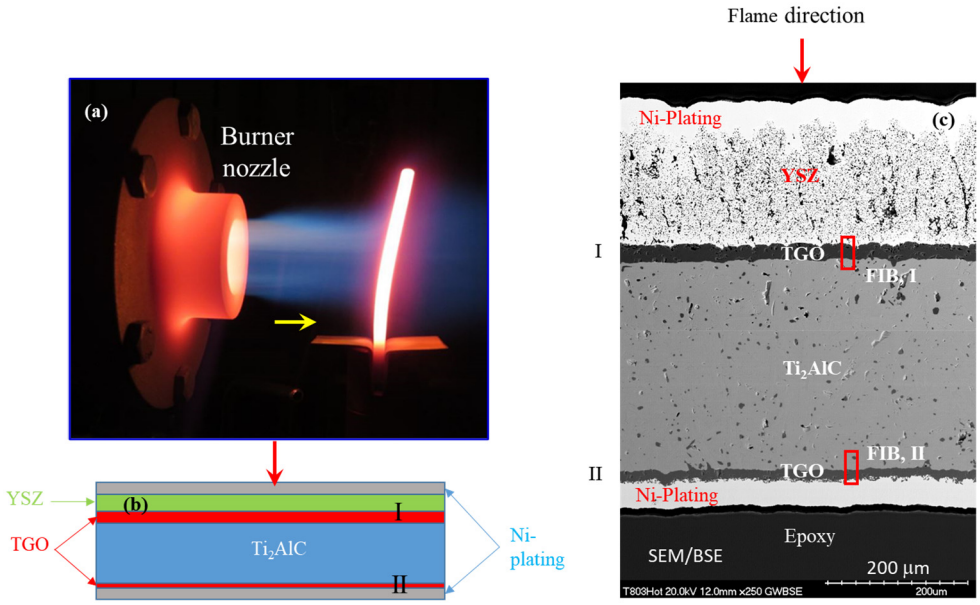


**Figure 2.** Orientation of FIB samples at (I) front and (II) back sides of the sample. (**a**) Photograph of burner operation showing front side flame impingement. (**b**) Schematic of sample cross-section. (**c**) Montage of SEM/BSE cross-section images of the sample and scale showing the TBC-coated front side (I) and bare backside (II) after 500 h burner rig test at 1300 °C.

## 3. Results

### *3.1. FIB I) YSZ-Coated, Front Side*

#### 3.1.1. Overview

The TEM microstructure of the TBC-coated side of the test bar from the interfacial region "FIB, I" marked in Figure 2, is shown in Figure 3. The TBC-coated side of the test bar was not evenly FIB thinned over the YSZ region. Coarsened porosity was evident and heavily streaked from ion milling near the Ni-plate layer. The $Al_2O_3$ scale (TGO) showed typically dispersed micro-porosity toward the outer half of the scale, some associated with fine, nm-sized Ti- or Zr- rich precipitates. The $Ti_2AlC$ was faulted, but with no dislocations observed on this hot convex side. The YSZ was a mix of large, featureless, cubic grains, and smaller, heavily strained and faulted, believed to be ordered t" tetragonal. The monoclinic phase was not observed. The faulted grains contained lathe-shaped domains with primarily (100) boundaries, some having (110) facets. These fault arrays indicate ferro-elastic domains used to explain high toughness in the 7YSZ t′ phase [9]. The Moire' patterns from overlapping, slightly offset, or rotated variants, 20–100 nm wide, were also prevalent, consistent with imaging theory. The coarsened intergranular micro-porosity was ubiquitous; this derived from the desirable dispersed intragranular nano-porosity responsible for low thermal conductivity in PVD-type coatings. Local Fe-oxide particles, identified at the $Al_2O_3$ surface and in the YSZ, may indicate a processing contamination issue. Iron impurities in our PS-PVD coatings had not typically been seen before.

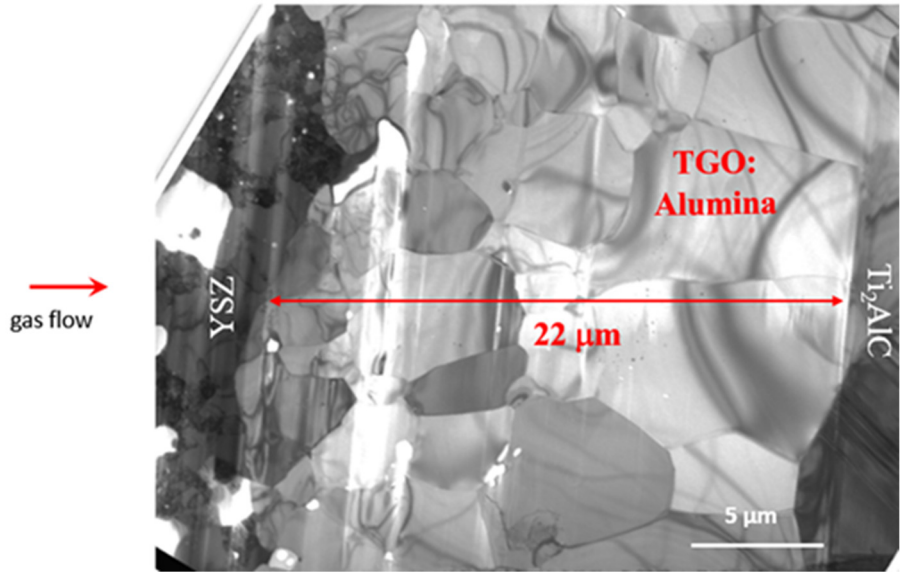


**Figure 3.** TEM Overview of the front side, FIB section I: TBC on the left, Ti2AlC MAX phase on the right. Avg. scale thickness from the prior SEM study was 22 µm, as shown (500 h at 1300 °C).

3.1.2. Microstructures

The first image (Figure 3) shows the ~22 µm thickness of the $Al_2O_3$ scale (TGO) at the front burner side: also present in this foil was a small amount of the adjoining YSZ of the thermal barrier coating on the left and the $Ti_2AlC$ MAX phase substrate on the right. The alumina grains (columnar) are on the order of 5 µm wide at the $Ti_2AlC$ interface and slightly smaller (equiaxed), ~3 µm, at the YSZ interface. More detail is presented in Figure 4. The $Al_2O_3$ -$Ti_2AlC$ interface was very clean and intact (Figure 4b). An array of long planar faults was apparent in a $Ti_2AlC$ grain, reflective of the basal faulting that may occur in MAX phases to accommodate stoichiometric variations, discussed later. The image in Figure 4a is from the central portion of the $Al_2O_3$ scale. It shows a small amount of intragranular porosity, generally finer than the intergranular pores displayed at lower magnification. Many of the pores were seen to be associated with dark nanoparticles, all quite fine, in the order of 100 nm. Similar pore-metal features were observed previously for alloy oxidation and may be typical of alumina scales. The white particle in the STEM image (Figure 5) showed high Y, Zr content (Figure 5b), with a small Fe peak and Cu from the support grid. The Y, Zr implies some diffusion from the TBC to the internal region of the scale. By comparison, EDS analysis of the featureless scale revealed only Al, O peaks (not shown). In addition, occasional light grey grains in the TBC match contrast with those at the $Al_2O_3$ scale interface and are believed to be Fe-rich oxide, as indicated by the EDS. The TGO/YSZ interface is shown in Figure 6a–d, with YSZ, $Al_2O_3$, and a few Fe-rich grains at the interface. These were likely iron-oxide grains formed due to spurious Fe-contamination during coating processing.

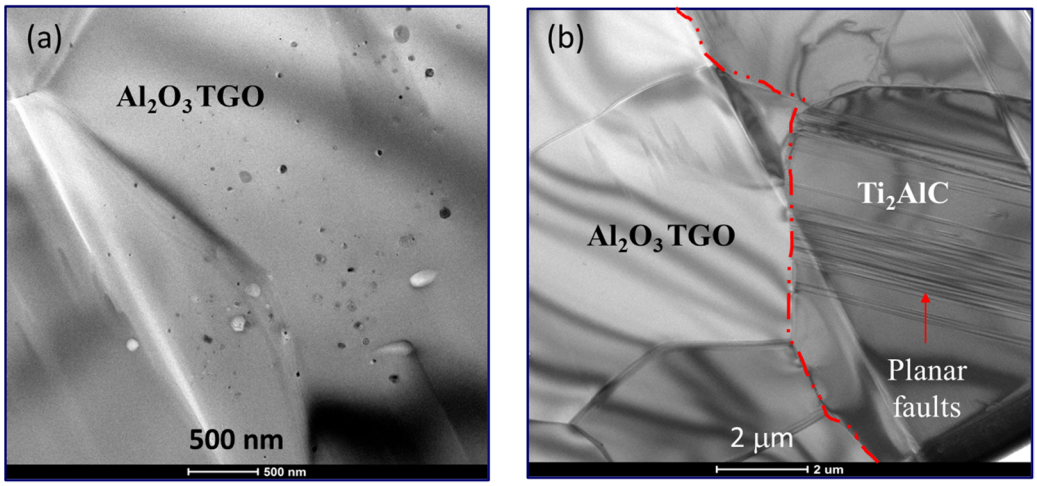


**Figure 4.** Features in $Al_2O_3$ TGO (I): (**a**) Fine 50 nm, dispersed intragranular porosity (light) and particles (dark) in $Al_2O_3$ grains near TBC; (**b**) clean, intact $Al_2O_3/Ti_2AlC$ interface (dashed red line) and ~20 closely spaced, highly aligned linear faults in the $Ti_2AlC$ grain.

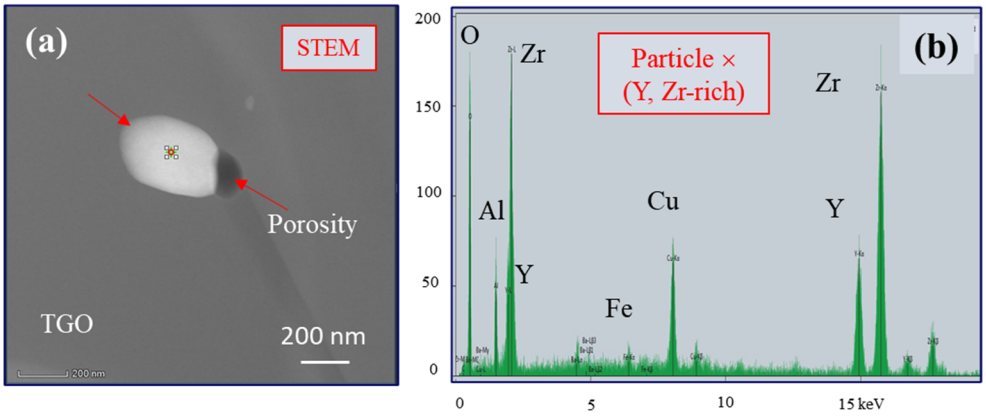


**Figure 5.** (**a**) STEM image and (**b**) EDS spectra of Zr(Y) rich particle embedded in $Al_2O_3$ (I) grain.

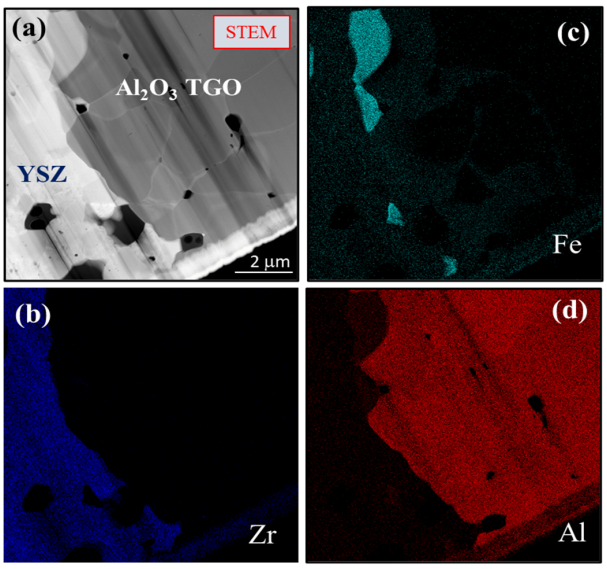


**Figure 6.** STEM image (**a**) of the TBC/TGO interface (I): elemental rasters (**b**–**d**) show Fe-rich particles at interface (500 h at 1300 °C).

The images in Figure 7 show the YSZ TBC region, which was generally a mosaic of 1–2 μm "clear" (C) and adjacent smaller, heavily faulted grains (F). The "feathery" nature of the YSZ columns appears to have sintered away. Large 1–2 μm intergranular pores and finer 0.1–0.2 μm pores were prevalent. The faulted grains are also replete with a high density of strain contours, consistent with transformation stresses. Figure 8a presents the SADP of a clean grain (C) and yields a clean cubic pattern for the $ZrO_2$ fluorite [110] zone axis. Since no (112) reflections are present in this zone axis, no information is obtained regarding the ordered tetragonal phases. A faulted grain (F), also produced *a "cubic"* [100] zone axis SADP with {100} and {110} reflections present (Figure 8b). This zone axis also showed a multitude of additional reflections. The latter were probably related to two twinned variants of a tetragonal daughter phase with respect to the cubic parent phase. Figure 9 presents an assemblage of lathes, believed to be ferro-elastic tetragonal domains. Such arrays can minimize strain energy under stress [9,10]. The <100>, <110> fault planes were seen as domain boundaries, with the FFT zone axis as [100] for the central grain. Another HRTEM image, Figure 9b, revealed multiple parallel lathes of the YSZ phase, ~20 nm wide. While the center lath appeared featureless, the two bordering it exhibited similar cross-hatch patterns, in colonies, with some resemblance to Moire's fringes. It is speculated that similar overlapping tetragonal colonies make up these structures. Tetragonal YSZ has nearly identical a, c unit cell dimensions, but varying orientations due to oxygen ion shifts along the z-axis [11]. HRTEM images were obtained near that region and produced a nearly orthogonal lattice structure and corresponding FFT diffraction pattern (Figure 10). The nodes along ⟨100⟩ (Figure 10b) show a spacing of ~0.5 nm (5 Å), approximating the unit cell dimension of 5.1 Å.

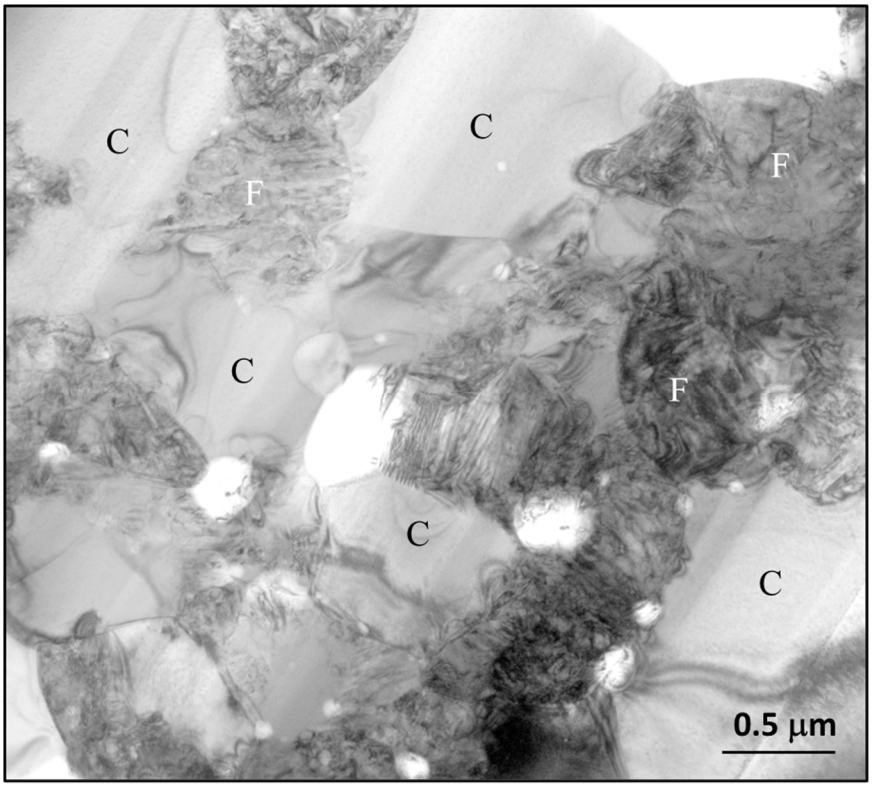


**Figure 7.** TEM image of cubic clear (C) and tetragonal "faulted" (F) submicron YSZ grains in the TBC.

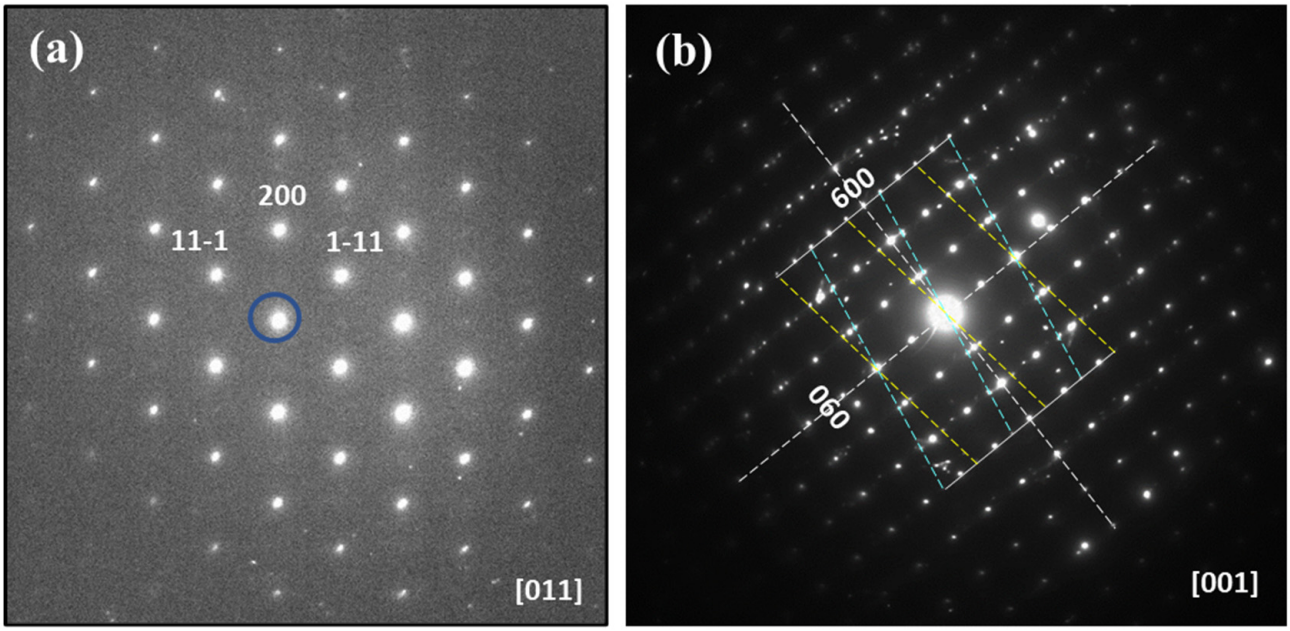


**Figure 8.** SADP's of (**a**) clear (C) [011], (beam marked by **O**) and (**b**) faulted (F) [001] YSZ grains (from Figure 7a,b), the latter showing many extra reflections probably related to variants of t″ domain orientation. In (**b**), the parent phase is shown as an orthogonal grid of {200} reflections. Extra reflections appear to arise from two twin variants, marked by the yellow and aqua dashed grids, slightly off-zone. The trace of possible twin habit planes, shown as orthogonal [200] and [020] axes ($a_0$ for YSZ is 5.1 Å for the cubic parent phase and indistinguishable from tetragonal).

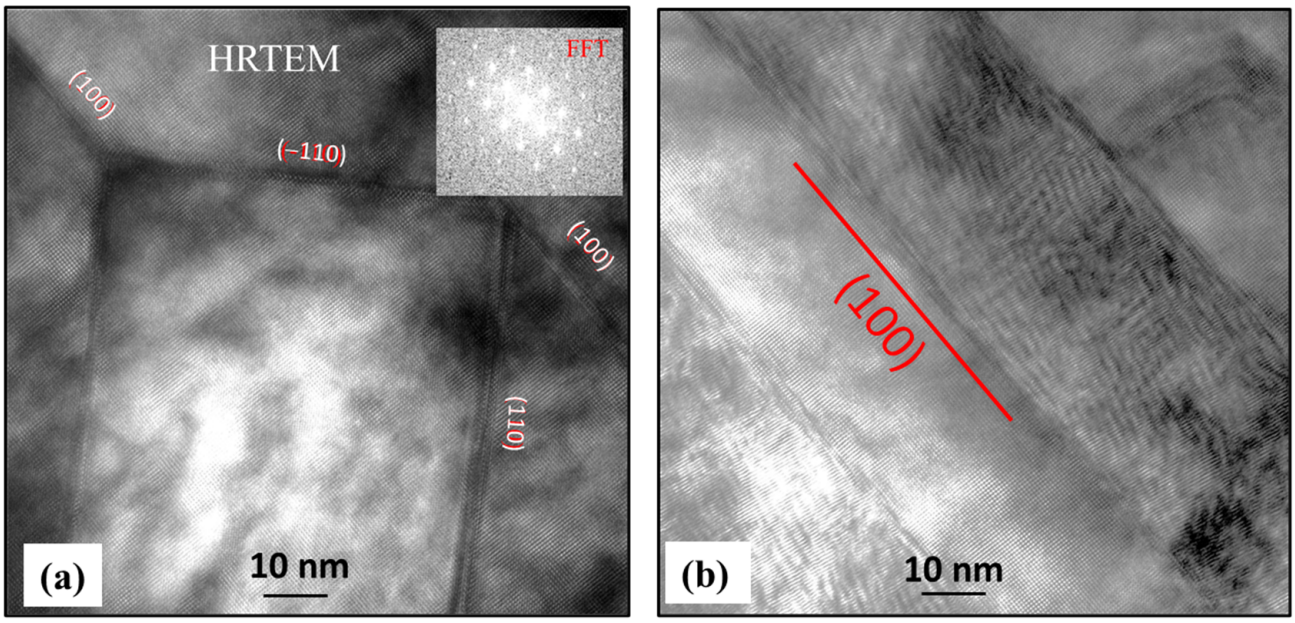


**Figure 9.** HRTEM images of ferro-elastic domain boundaries in faulted (F) grains; inset: fast Fourier transform of lattice image. Domain boundaries exhibit {100} and {110} nature with 45° or 90° angles of inclination between themselves; (**b**) other domains to the left of (**a**).

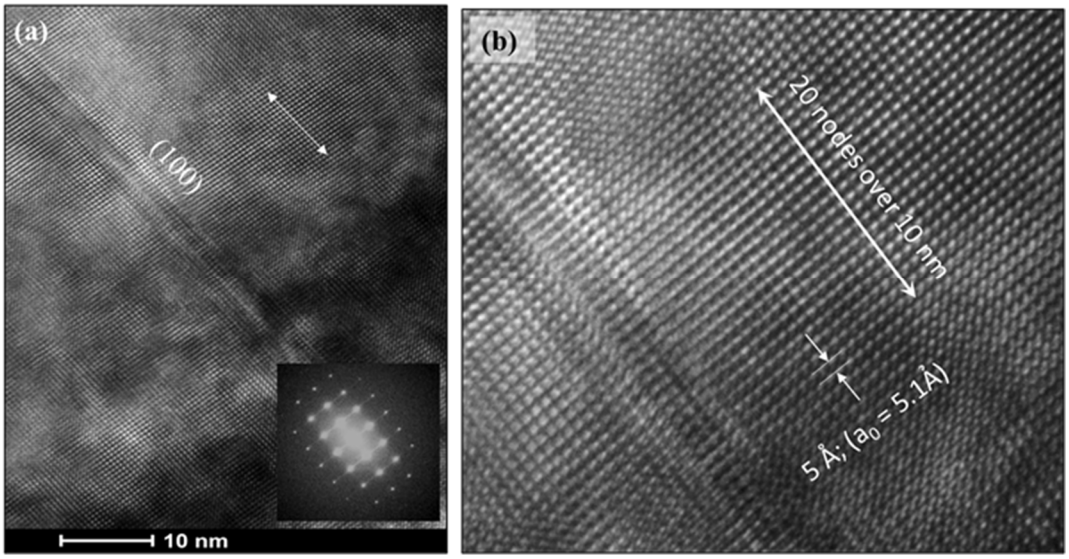


**Figure 10.** HRTEM images of domain boundary above Figure 9a; (**a**) inset: fast Fourier transform of lattice image; (**b**) enlargement showing node spacing of 5 Å, corresponding to 5.1 Å lattice spacing for {100} planes.

### *3.2. FIB II) Uncoated, Backside*

#### 3.2.1. Overview

The TEM microstructure of the uncoated backside of the test bar is from the interfacial region marked "FIB, II" in Figure 2. Prior SEM had shown outermost filamentary, exposed alumina grains or Ti-rich scale remnants. However, this surface was not protected enough during FIB milling and appeared to be just out of the span of the foil. Within the retained scale, columnar TGO $Al_2O_3$ grains are nicely imaged, with more equiaxed grains and porosity toward the gas surface. A small number of fine 25 nm-rich spherical particles were dispersed. Some very small Fe-rich particles were observed at the edge of 50 nm nanopores. The $Al_2O_3$—$Ti_2AlC$ interface appeared intact and exceptionally clean. No significant detachment or distress at the interface was indicated. Interface faceting followed $Al_2O_3$ grains. The $Ti_2AlC$ substrate on this end (concave bending) was replete with dislocations and MAX phase stacking faults on the basal (0001) plane. The $Al_2O_3$ impurity phase, commonly observed as a processing artifact in Al-MAX phases, was conclusively identified by EDS.

#### 3.2.2. Microstructures, FIB II—Back

Figure 11 presents the uncoated backside of the $Ti_2AlC$ sample. The $Al_2O_3$ TGO grew to ~14 μm; this was less than the front face because of the lower backside temperature of ~1216 °C. The $Al_2O_3$ grains were again columnar and presented a very clean, faceted interface with $Ti_2AlC$. The EDS of a grain interior (Figure 12a) showed only Al and O, as well as for a particle (P) in the MAX phase. (Similar clean Al, O EDS spectra were obtained for the front side, I, featureless TGO regions). The SADP's of the TGO (Figure 12c,d for grains marked A and B) were consistent with trigonal (pseudo-hexagonal) corundum, a = 4.8 Å, c = 12.9 Å, near Z.A. [21–1] and [481], respectively. Figure 13a shows very fine nm-size TGO particles in the vicinity of the triple point in Figure 11, yielded EDS showing Ti (Figure 13b), while that (F) associated with a pore contained Fe (Figure 13c).

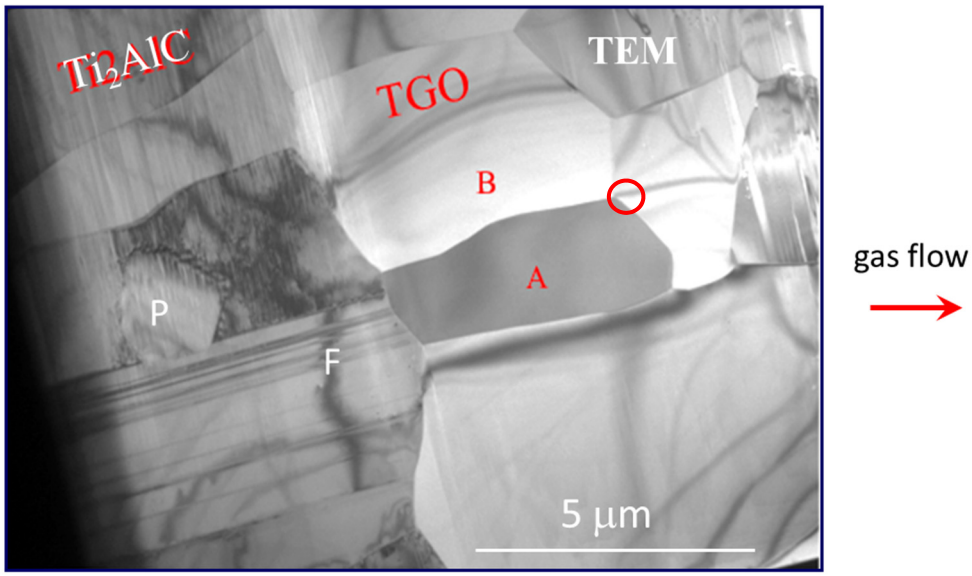


**Figure 11.** FIB section II: TEM image of the *backside* of the burner sample. Clean, intact $Ti_2AlC$—$Al_2O_3$ interface. Columnar TGO grains at the interface and equiaxed at gas side; planar faults (F) and included $Al_2O_3$ particle (P) in $Ti_2AlC$ (500 h at 1216 °C).

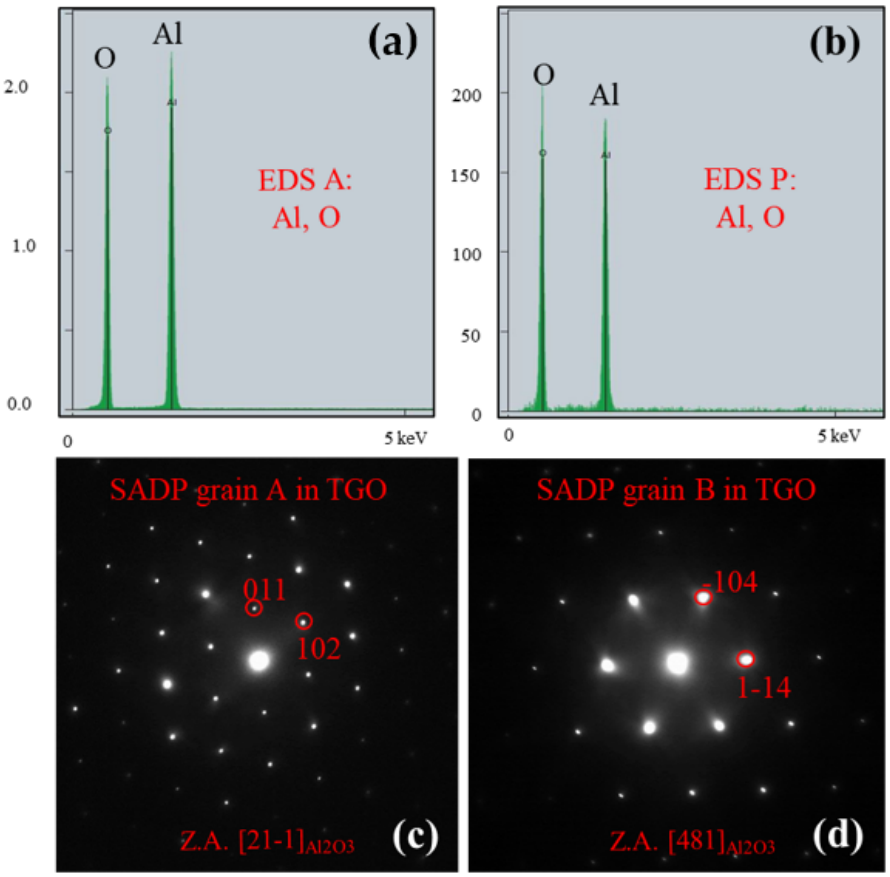


**Figure 12.** EDS spectra of (**a**) TGO grain (A) and (**b**) imbedded particle (P) in Figure 11. (**c**) hkl [21–1] and (**d**) [481] Z.A. SADP of TGO grains (A) and (B) in Figure 11. Hexagonal $Al_2O_3$: $a_0$ = 4.8 Å, c = 12.9 Å.

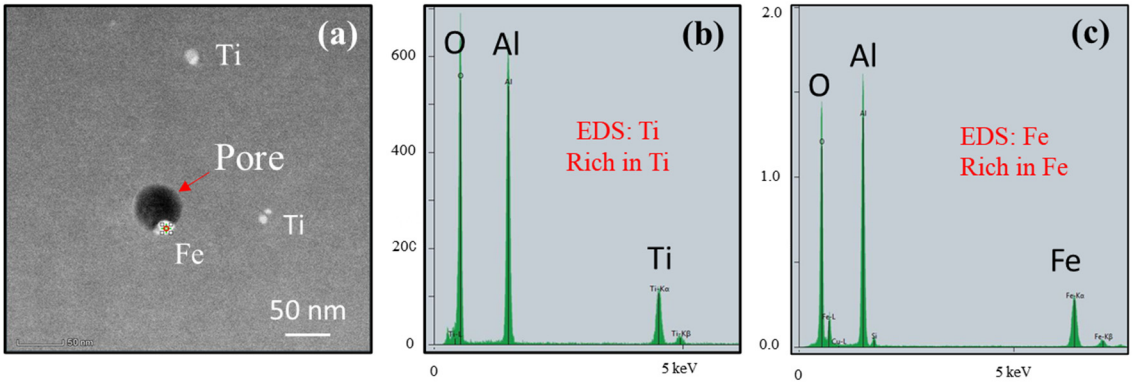


**Figure 13.** (**a**) $Al_2O_3$ TGO triple point region marked O in Figure 11, showing fine ~25 nm Ti- and Fe-rich particles. EDS spectra of Ti (**b**) and Fe (**c**) particles.

Figure 14 shows the interior of $Ti_2AlC$ grains having a dispersion of dislocations, consistent with reported bending deformation at temperature. Other grains contained long parallel fault features (Figure 15a). The EDS spectra for $Ti_2AlC$ (T; Figure 15b) again produced a clean Ti, Al, C result. Accordingly, the SADP of the grain interior (X; Figure 15c) shows only the $Ti_2AlC$ hexagonal MAX phase, a = 3.1 Å, c = 13.7 Å, Z.A. = [210]. Whereas, at faulted regions (Y; Figure 15d), extra reflections appeared for the basal plane along —presumably the fault plane. This corresponds to basal plane stacking sequence variations that can occur due to various $Ti_xAl_yC_z$ stoichiometries. Here, the Al atoms are arranged on the c-plane, every third layer for the 211 compound, then every fourth and fifth layer for decreasing Al stoichiometries corresponding to 312 $Ti_3AlC_2$ and 413 $Ti_4AlC_3$ cells [12,13]. The latter were equivalent to c-plane spacings, respectively, of 4/3 and 5/3 that of the basic 3-layer cell having 211 $Ti_2Al_1C_1$ stoichiometry. Increased d-spacings produce inversely decreased reciprocal lattice spacing. In Figure 15d, we have minor reflections produced at the fault boundary (Y), along the c-axis, with $(007)_{fault}$ superposed on the $(006)_{211}$ reflection. Thus, the d-spacing is 7/6 that of the $Ti_2AlC$ 211 phase, or has 3.5 layers/cell. This value is midway between 211 and 312 MAX phase cells. The fault stoichiometry can therefore be surmised to be $Ti_{2.5}AlC_{1.5}$ or $Ti_5Al_2C_3$.

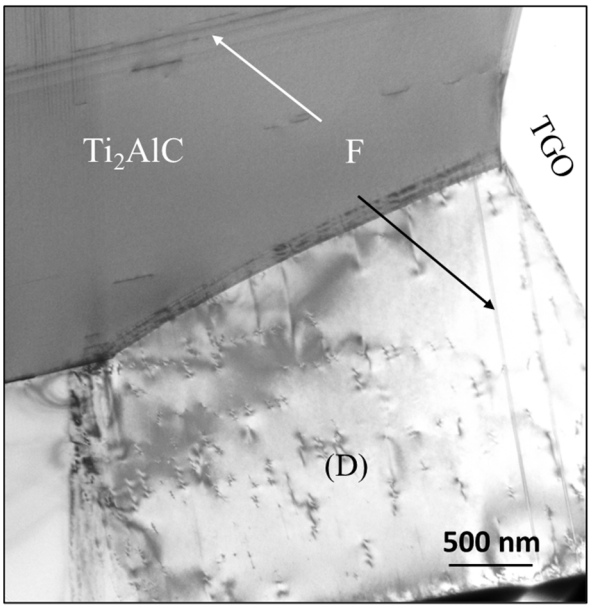


**Figure 14.** $Ti_2AlC$ grains with planar faults (F) and irregular dislocations (D).

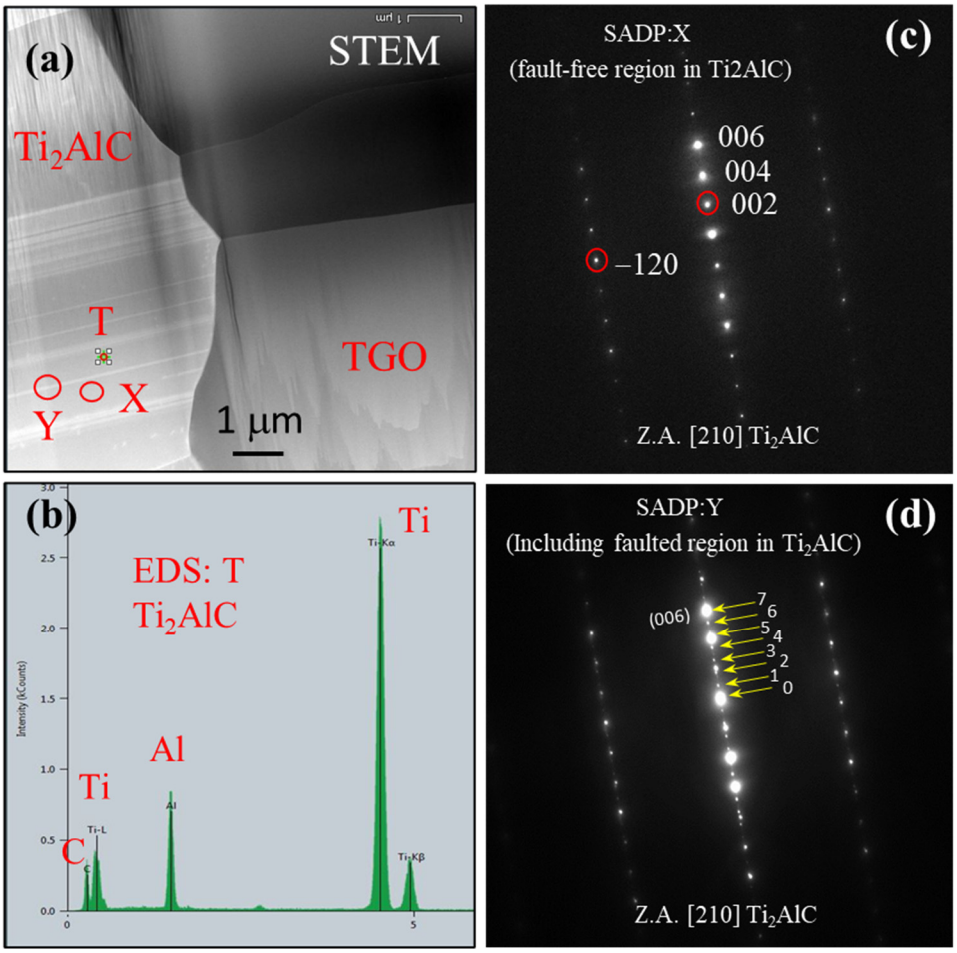


**Figure 15.** STEM image showing (**a**) the clean, intact $Ti_2AlC$—$Al_2O_3$ interface, circles mark SADP; (**b**) EDS of the $Ti_2AlC$ phase (T); (**c**) [210] Z.A SADP of the fault-free region (X), circles mark the primary reflections; and (**d**) extra spots in the SADP of the faulted plane (Y). The fine spots (yellow arrows) are regularly spaced at 1/7 (006), indicating a d-spacing of 7/6 $d_{(001)}$, with $Ti_2AlC$: Hexagonal, $a_0$ = 3.1 Å, c = 1 3.7 Å.

## 4. Discussion

### *4.1. PS-PVD YSZ TBC*

Table 1 compares the XRD phase analyses of this coating with those from an extensive annealing study by Witz et al. [14], both determined from a Rietveld full XRD pattern fitting. Both indicate a thermally activated transition from the quenched-in metastable **t′** tetragonal, with quenched-in Y content, into the equilibrium, low Y tetragonal (**t**) + high Y cubic (**c**). Those general trends were repeated from earlier studies. However, a much higher amount of cubic (28–86% compared to 4–37%) is shown throughout for our coating, as well as an almost negligible 0.5% monoclinic after aging at 1300 °C. Given the TEM structures showing nearly equal amounts of cubic and faulted tetragonal grains (Figure 7), one can only surmise that the faulted tetragonal structures exhibit a 'cubic' nature in XRD analyses. Initially, (**t**) identification was based primarily on {400} peak splitting due to increased c/a. Now, the c-axis vacancy ordering that gives rise to the tetragonality appears to be occurring without a change in lattice constants. Thus, ferro-elastic domains appear in HRTEM imaging but without the classic $(400)_c$ peak-splitting in X-ray diffraction patterns. The proximity and distribution of the "clear" and faulted grains are consistent with Y partitioning to cubic and away from tetragonal, with phase separation.

**Table 1.** Summary of YSZ-coating phases after various thermal aging treatments. Rietveld XRD full pattern fitting of for t′, t, c, and m YSZ (wt. %), with corresponding compositions ($YO_{1.5}$ %): (a) from Witz et al., APS. [14] (b) this study, PS-PVD [5].

| | | wt. % | | | | $YO_{1.5}$ % | | |
|---|---|---|---|---|---|---|---|---|
| °C | Hours | t′ | t | c | m | t′ | t | c |
| (a) as deposited | | 88.0 | 7.5 | 3.7 | | 8.0 | 5.0 | 10.7 |
| 1100 | 850 | 48.4 | 39.5 | 12.1 | | 7.0 | 5.3 | 13.8 |
| 1200 | 1000 | 27.1 | 49.2 | 23.7 | | 7.1 | 3.4 | 15.8 |
| 1300 | 1000 | 0.0 | 35.9 | 37.4 | 26.7 | | 4.6 | 15.3 |
| (b) 926 | 0.17 | 67.9 | | 27.9 | 3.0 | 9.8 | | 13.5 |
| 1200 | 500 | 0.0 | 31.2 | 64.0 | | | 3.7 | 14.7 |
| 1300 | 500 | 0.0 | 11.3 | 86.0 | 0.5 | | 3 | 9.4 |

The Y content in the various phases was estimated from Rietveld lattice parameters and calibration formulas from the literature. The results based on a c/a calibration are also shown in Table 1. The present coating is seen to have higher as-sprayed $YO_{1.5}$ content in the cubic phase [5] compared to that of Witz et al. [14] (n. the 926 °C/0.17 h condition here is considered to be essentially as-sprayed). The cubic results from the two studies are similar after 1100 °C and 1200 °C exposures, at 13–15%, but lower here after 1300 °C, at 9% vs. 15%.

According to the study by Azzopardi, et al., 2004, [15] for PVD t´ YSZ coatings, the initial metastable tetragonal **t′** phase transforms into a mixture of yttria-poor tetragonal phase **t** and yttria-rich cubic **c** phase upon thermal aging, as described previously over many years. However, on cooling, the **c** phase can further transform into a yttria-rich **t″** phase [16] that has tetragonal symmetry but cubic dimensionality. The yttria-poor **t** phase does not transform to monoclinic, presumably because of the fine grain size and stress constraints on the transformation. That **t** phase should not be considered 'non-transformable **t′**, e.g., upon grinding. To make matters more complex, these **t** + **c** phases evolved into a fine, 10 nm banded domain structure.

It is, therefore, postulated that the present study exhibits faulted **t″** YSZ grains, transformed from cubic parent grains on cooling. A domain structure reflects the three different tetragonal variants possible from a cubic parent, usually shown by dark-field imaging using the (112) extra spots. Here they are shown as domain boundaries in HRTEM, with a node spacing of 5 Å. But the low Y content (9%) is more representative of **t″** rather than equilibrium phase-separated cubic. Martensite has not formed due to the small grain size of any parent structures and was not obvious in the TEM microstructures or previous XRD. The 'clear' cubic grains have retained the equilibrium **c** structure. Further subtleties and delineations are beyond the scope of this work. The presence of these domains, even after extensive thermal exposure, probably contributes to the overall mechanical durability of the coating upon cycling, as does the absence of the disruptive monoclinic transformation.

### *4.2. $Al_2O_3$ TGO*

The alumina scales exhibited typical inner columnar grains and more equiaxed outer grains. At the frontside YSZ interface, some Fe-rich scales were observed and presumed to result from some Fe-rich chamber contamination during the initial plasma spray conditions before deposition. None were seen on the backside. Small included Zr(Y) particles were observed underneath the YSZ coating. Intergranular porosity was present in the equiaxed region but absent in the columnar region. The interior of the grains was essentially featureless, except for minute amounts of fine, 25–50 nm pores and Fe or Ti-rich particles. Again, the source of the Fe is believed to be migration from initial PSD-PVD contaminants, whereas the Ti indicates some minute presence from the $Ti_2AlC$ substrate. Considering the 2:1 Ti:Al ratio in the 211 MAX phase, it is remarkable that only this small amount of Ti enters into the scale. This is thought to be a vestige of initial Ti-rich transient oxidation before a healing layer of $Al_2O_3$ is formed. Oxidation of bare $Ti_2AlC$ in high-temperature

air or oxygen is well known to produce a $TiO_2$ or $TiAl_2O_4$ initial scale before a healing, rate-controlling scale of $Al_2O_3$ is formed underneath. The exclusion of the typical $TiO_2$ transient outer layers here suggests that low $pO_2$ pre-oxidation, expected during initial PS-PVD processing, plays a beneficial role here. The stable, long-term growth of $Al_2O_3$ at 1300 °C is confirmed by the chemical and phase purity of the scale at the $Ti_2AlC$ interface. The $Al_2O_3$–$Ti_2AlC$ interfacial regions appeared fully intact, smooth, and atomically bonded (unfortunately, the filamentary $Al_2O_3$ TGO surface resulting from scale volatility on the exposed backside [5] was not included in the optimal portion of this FIB section).

### *4.3. $Ti_2AlC$ Substrate*

The MAX phase substrate was fine-grained and exhibited a typical $Al_2O_3$ processing inclusion but little chemical/phase diversity. Planar, intragranular (basal plane) faults were common, often nearly perpendicular to the $Al_2O_3$ –$Ti_2AlC$ interface. These are interpreted as a tendency toward local $Ti_3AlC_2$ chemistry to accommodate reduced Al content. This mechanism allows for maintaining an intact MAX phase–alumina interface without a distinct depletion layer, as is common for alumina-forming alloys or $Cr_2AlC$. It is perhaps an indication of the ability of the $Ti_xAlC_y$ MAX phases to supply Al rapidly enough through the bulk of the substrate along basal planes to support the growing scale. Preferential Al diffusion along basal planes has been proposed to explain preferential $Al_2O_3$ scale formation and improved oxidation behavior for textured $Ti_2AlC$, $Ti_3AlC_2$, and $Ti_3(Si,Al)C_2$ MAX phases [17–20]. Here, the MAX phase basal planes were aligned perpendicular to the hot pressing direction and served to enhance Al diffusion toward side faces (TSS) in comparison to top faces (TTS). The present SADP diffraction results along [001] on a basal plane fault (Figure 15) suggest a fault stoichiometry of $Ti_{2.5}AlC_{1.5}$. Dislocations were also evident as an indication of the macroscopic plastic deformation that occurred in this sample progressively throughout the 500 h test. That was manifested as a 2.3 mm cord-wise deflection across the 6.8 cm burner sample length, as bent by the gas flow [8]. Dislocations and plastic deformation are consistent with high creep rates reported for MAX phase structures above 1200 °C [21].

## 5. Summary

The schematic in Figure 16 (not to scale) shows some key features derived from this FIB/STEM study of YSZ coated $Ti_2AlC$ MAX phase after Mach 0.3 burner rig testing at 1300 °C surface temperature for 500 h. The FIB/STEM samples were obtained at the coated front and bare backside. There was no indication of TGO or TBC failure. The YSZ was a mix of 1–2 μm "clean" and 0.5–1 μm "faulted" grains with nm-size domains. The domains produced complex SADP; HRTEM revealed {100} and {110} domain boundaries, while XRD had identified primarily "cubic cell" structures. These ferro-elastic domains are believed to represent high Y, tetragonal **t"** YSZ variants generated from the cubic phase on cooldown. No martensite was observed, presumably due to mechanical constraints of fine grain size. The complexity of aged YSZ coatings is a topic requiring intensive study to be fully conclusive. The presence here of ferro-elastic **t"** domains are expected to be beneficial in the same manner as those widely documented in metastable, "non-transformable", as-sprayed **t′** tetragonal domains. Still, the thermal expansion matching of this YSZ-TGO-MAX phase system presents the largest positive factor for long-term, high-temperature, cyclic durability. The loss of the strain-compliant PVD "feather" grain structure during sintering, useful for TBC's on superalloys operated at lower temperatures, has apparently not diminished this durability.

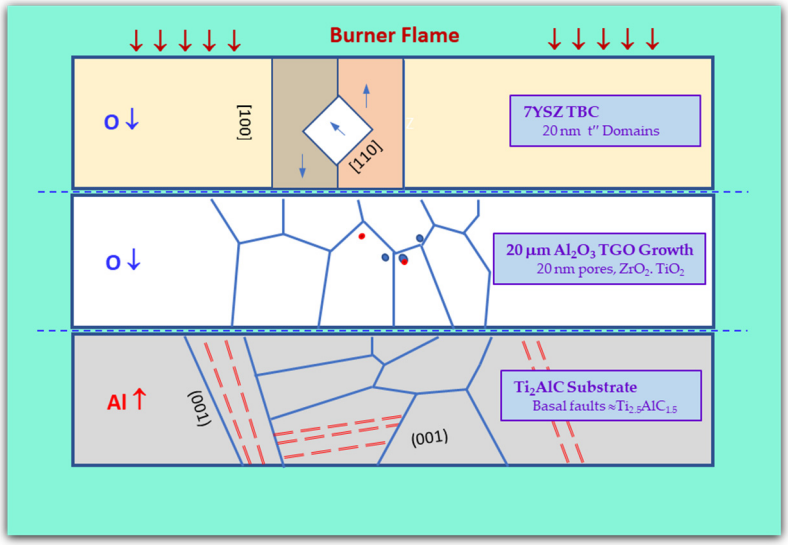


**Figure 16.** Schematic of substructural features revealed by FIB/STEM for a novel YSZ/$Ti_2AlC$ system after aggressive oxidation in a burner test, flame direction, arrows (not to scale). Ferro-elastic t'' tetragonal domains in the TBC; adherent, inward growing, columnar α-$Al_2O_3$ grains, with only minor nm pores or particle defects, red/blue spots; and the $Ti_2AlC$ MAX phase substrate, with Al-poor stacking faults, red dashes, but no Al depletion zone.

The TGO was essentially α-$Al_2O_3$, with a duplex structure of outer ~3 µm equiaxed grains (with intergranular porosity) and inner columnar 5 µm grains. The latter showed minimal entrapped fine 25–50 nm porosity and Zr(Y), Fe, or Ti-rich particles. Little interaction with the YSZ was observed. Unfortunately, no information was obtained at the bare backside scale-gas interface because it was outside the span of the FIB section. That surface had exhibited volatility issues (grain boundary etching, filamentary α-$Al_2O_3$, $TiO_2$ removal) in previous SEM studies.

The scale maintained a perfectly intact interface with the $Ti_2AlC$ substrate, with no evidence of interfacial porosity or chemical/phase variations. The $Ti_2AlC$ substrate exhibited no depletion zone but rather numerous crystallographic faults along the basal plane of the hexagonal structure, often extending deep into the grains. These are believed to offer a means of depleting Al by forming a crystallographic planar defect having lower Al stoichiometry in the hexagonal stacking of the $Ti_{n+1}AlC_n$ MAX phase series. This has wide implications for Al depletion mechanisms in the high-temperature oxidation of the $Ti_{n+1}AlC_n$ family of MAX phases.

In closing, some representative features of the YSZ TBC, α-$Al_2O_3$ TGO, and $Ti_2AlC$ MAX phase substrate have been illustrated by FIB/STEM techniques. This oxidized system represented extremely high durability in a long-term 1300 °C burner test. Many of the features were proposed to support the assumptions underlying durability, while others may simply be innocuous details. Both may provide a useful reference in future studies.

**Author Contributions:** J.L.S. conceived and organized the research, and prepared the manuscript; A.G. performed the transmission electron microscopy; B.J.H. produced the coated sample; M.D.C. performed the high-velocity burner rig test. All authors have read and agreed to the published version of the manuscript.

**Funding:** These studies were supported by the NASA Fundamental Aeronautics Program.

**Data Availability Statement:** Not applicable.

**Acknowledgments:** The authors gratefully acknowledge Wayne Jennings for producing the FIB sections.

**Conflicts of Interest:** The authors declare no conflict of interest.

## References


1. Darolia, R. Thermal barrier coatings technology: Critical review, progress update, remaining challenges and prospects. *Int. Mater. Rev.* **2013**, *58*, 315–348. [CrossRef]
2. Pint, B.A.; Wright, I.G.; Brindley, W.J. Evaluation of Thermal Barrier Coating Systems on Novel Substrates. *J. Therm. Spray Technol.* **2000**, *9*, 198–203. [CrossRef]
3. Smialek, J.L.; Harder, B.J.; Garg, A. Oxidative durability of TBCs on $Ti_2AlC$ MAX phase substrates. *Surf. Coat. Technol.* **2016**, *285*, 77–86. [CrossRef]
4. Gonzalez-Julian, J.; Go, T.; Mack, D.E.; Vaßen, R. Thermal cycling testing of TBCs on $Cr_2AlC$ MAX phase substrates. *Surf. Coat. Technol.* **2018**, *340*, 17–24. [CrossRef]
5. Smialek, J.L.; Cuy, M.D.; Harder, B.J.; Garg, A.; Rogers, R.B. Durability of YSZ coated $Ti_2AlC$ in 1300 °C high velocity burner rig tests. *J. Am. Ceram. Soc.* **2020**, *103*, 7014–7030. [CrossRef]
6. Gonzalez-Julian, J.; Mauer, G.; Sebold, D.; Mack, D.E.; Vassen, R. $Cr_2AlC$ MAX phase as bond coat for thermal barrier coatings: Processing, testing under thermal gradient loading, and future challenges. *J. Am. Ceram. Soc.* **2020**, *103*, 2362–2375. [CrossRef]
7. Smialek, J. L Compiled furnace cyclic lives of EB-PVD thermal barrier coatings. *Surf. Coat. Technol.* **2015**, *276*, 31–38. [CrossRef]
8. Smialek, J.L.; Cuy, M.D.; Harder, B.J.; Garg, A.; Rogers, R.B. *Durability of YSZ Coated $Ti_2AlC$ in 1300 °C Mach 0.3 Burner Rig Tests*; NASA Technical Memorandum NASA/TM-2020-220380; NASA: Washington, DC, USA, 2020. Available online: https://ntrs.nasa.gov/citations/20200001406 (accessed on 10 April 2023).
9. Virkar, A.V.; Matsumoto, R.L.K. Ferroelastic Domain Switching as a Toughening Mechanism in Tetragonal Zirconia. *J. Am. Ceram. Soc.* **1986**, *69*, C224–C226. [CrossRef]
10. Srinivasen, G.; Jeu, J.F.; Kuo, S.Y.; Virkar, A.V. Ferroelastic Domain Switching in Polydomain Tetragonal Zirconia Single Crystals. *J. Am. Ceram. Soc.* **1989**, *72*, 2098–2103. [CrossRef]
11. Miller, R.A.; Smialek, J.L.; Garlick, R.G. Phase stability in plasma-sprayed, partially stabilized zirconia-yttria. *Sci. Technol. Zirconia* **1981**, *3*, 241–253.
12. Radovic, M.; Barsoum, M.W. MAX phases: Bridging the gap between metals and ceramics. *Am. Ceram. Soc. Bull.* **2013**, *92*, 20–27.
13. Barsoum, M.W.; El-raghy, T. The MAX Phases: Unique New Carbide and Nitride Materials. *Am. Sci.* **2001**, *89*, 334–343. [CrossRef]
14. Witz, G.; Shklover, V.; Steurer, W.; Bachegowda, S.; Bossmann, H.P. Phase evolution in yttria-stabilized zirconia thermal barrier coatings studied by rietveld refinement of X-ray powder diffraction patterns. *J. Am. Ceram. Soc.* **2007**, *90*, 2935–2940. [CrossRef]
15. Azzopardi, A.; Mevrel, R.; Saint-Ramond, B.; Olson, E.; Stiller, K. Influence of aging on structure and thermal conductivity of Y-PSZ and Y-FSZ EB-PVD coatings. *Surf. Coat. Technol.* **2004**, *177*, 131–139. [CrossRef]
16. Yashima, M.; Kakihana, M.; Yoshimura, M. Metastable-stable phase diagrams in the zirconia-containing systems utilized in solid-oxide fuel cell applcation. *Solid State Ion.* **1996**, *86*, 1131–1149. [CrossRef]
17. Xu, L.; Zhu, D.; Liu, Y.; Suzuki, T.S.; Kim, B.; Sakka, Y.; Grasso, S.; Hu, C. Effect of texture on oxidation resistance of $Ti_3AlC_2$. *J. Eur. Ceram. Soc.* **2018**, *38*, 3417–3423. [CrossRef]
18. Li, X.; Xie, X.; Gonzalez-Julian, J.; Malzbender, J.; Yang, R. Mechanical and oxidation behavior of textured $Ti_2AlC$ and $Ti_3AlC_2$ MAX phase materials. *J. Eur. Ceram. Soc.* **2020**, *40*, 5258–5271. [CrossRef]
19. Li, X.; Xie, X.; Gonzalez-Julian, J.; Yang, R.; Schwaiger, R. Oxidation and creep behavior of textured $Ti_2AlC$ and $Ti_3AlC_2$. *J. Eur. Ceram. Soc.* **2022**, *42*, 364–375. [CrossRef]
20. He, G.; Zhang, X.; Wang, W.; Ma, K.; Zuo, J.; Li, M.; Liu, C.; Xu, J. Anisotropy oxidation behavior and mechanism of textured $Ti_3(Si,Al)C_2$ ceramic. *Nat. Mater. Degrad.* **2023**, *3*, 19. [CrossRef]
21. Sun, Z.M. Progress in research and development on MAX phases: A family of layered ternary compounds. *Int. Mater. Rev.* **2011**, *56*, 143–166. [CrossRef]